



Cite this: DOI: 10.1039/d0nj02165b

# Highly selective hydrogenation of halogenated nitroarenes over Ru/CN nanocomposites by *in situ* pyrolysis†

 Shengnan Yue,<sup>a</sup> Xueguang Wang,<sup>a\*</sup> Shaoting Li,<sup>a</sup> Yao Sheng,<sup>a</sup> Xiuqing Zou,<sup>a</sup> Xiongqiang Lu<sup>a</sup> and Chunlei Zhang<sup>\*b</sup>

A highly chemoselective and recyclable ruthenium catalyst for the hydrogenation of halogenated nitroarenes has been prepared *via* the simple *in situ* calcination of a mixture of melamine, glucose and ruthenium trichloride. Superfine Ru particles ( $2.3 \pm 0.3$  nm) were obtained and highly dispersed in the nitrogen-doped carbon matrix. The Ru/CN catalyst smoothly transforms a variety of halogenated nitroarenes to the corresponding haloanilines with high intrinsic activity (e.g. TOF =  $1333 \text{ h}^{-1}$  for *p*-chloronitrobenzene) and selectivity of more than 99.6%. Furthermore, through an analysis of the products in the reaction process, it was concluded that there are two parallel reaction pathways (a direct pathway and an indirect pathway) for the hydrogenation of aromatic nitro compounds over the Ru/CN catalyst, and the direct pathway was proved to be dominant in catalyzing the intermediates.

 Received 29th April 2020,  
 Accepted 16th June 2020

DOI: 10.1039/d0nj02165b

[rsc.li/njc](http://rsc.li/njc)

## 1. Introduction

As basic chemical raw materials and organic intermediates, aromatic amine and its derivatives play crucial roles in medicines, dyes, pesticides, and everyday chemical industries.<sup>1–5</sup> The main method of manufacturing aromatic amines is the reduction of the corresponding aromatic nitro compounds,<sup>6–8</sup> including chemical reduction,<sup>9</sup> electrolytic reduction,<sup>10</sup> and catalytic hydrogenation reduction.<sup>11,12</sup> However, from the perspectives of environmental protection and economic benefits, the traditional chemical reduction method applying Fe, FeS, Zn, or Na<sub>2</sub>S as the reductants<sup>13,14</sup> has been gradually eliminated due to the production of plenty of hazardous wastewater and the low yields. Meanwhile, the development of electrolytic reduction has also been limited by its high cost.<sup>15,16</sup> By contrast, catalytic hydrogenation has become the preferred option and has been widely utilized in preparing aromatic amine compounds owing to its high selectivity and less waste as well as easy post-treatment.<sup>17–19</sup>

The catalyst is one of the most crucial parameters determining the activity and selectivity of the hydrogenation reaction, and

catalysts can be simply divided into noble metal group and non-noble metal group catalysts. The noble metals with high catalytic activity and mild reaction conditions are mainly platinum,<sup>20,21</sup> palladium,<sup>2,22,23</sup> rhodium,<sup>24</sup> gold,<sup>16</sup> silver,<sup>25</sup> and ruthenium.<sup>26</sup> And the non-noble metals include nickel,<sup>27</sup> copper,<sup>28</sup> cobalt,<sup>29</sup> iron,<sup>30</sup> molybdenum,<sup>31</sup> and their oxides and alloys<sup>32,33</sup> which are low cost but require harsh reaction conditions such as high temperature and high pressure.<sup>18,34</sup> Currently, supported noble metal catalysts like platinum and palladium have been widely applied for the reduction of nitroarenes with H<sub>2</sub> as the reductant because of their excellent activity. Nevertheless, in the preparation of halogenated aromatic amines, the highly active metals platinum and palladium have a serious drawback – the superior hydrolytic activity of the carbon-halogen bond usually leads to dehalogenation, which produces many by-products and reduces the quality of the product. Ruthenium has been demonstrated to exhibit much higher selectivity in hydrogenation of the halogenated nitroarenes,<sup>35</sup> and its lower price and lower dehalogenation trend compared to Pt and Pd mean it has great potential in the chemoselective hydrogenation of halogenated nitroarenes.

The performance of a catalyst for the hydrogenation of halogenated nitroarenes depends not only on the kind of active metal but also on the properties of the support. It is generally accepted that the characteristics of the catalyst support, such as the strength, specific surface area, pore structure, and surface properties can remarkably affect the dispersion, morphology, and metal-support interaction of the active phase.<sup>36</sup> In addition, the size and shape of the active phase particles also play a

<sup>a</sup> State Key Laboratory of Advanced Special Steel, School of Materials Science and Engineering, Shanghai University, Shanghai 200444, China.  
 E-mail: wxg228@shu.edu.cn

<sup>b</sup> Education Ministry Key Lab of Resource Chemistry, Shanghai Key Laboratory of Rare Earth Functional Materials, College of Chemistry and Materials Science, Shanghai Normal University, Shanghai 200234, China.  
 E-mail: zhangchunlei@shnu.edu.cn

† Electronic supplementary information (ESI) available. See DOI: 10.1039/d0nj02165b

crucial role in the catalytic reduction.<sup>37</sup> These factors are inter-related and closely related to the performance of the catalyst in halogenated nitroarene reduction. Therefore, choosing an appropriate support in the preparation of an effective catalyst is of great significance. Many studies have shown that activated carbon materials could be successfully applied as supports for noble metal catalysts in the fine chemical industry due to their excellent thermal stability, strong acid and alkali resistance, and large specific surface area.<sup>38</sup> However, the active metal nanoparticles tend to be exuded from the support in the catalytic process because of the weak interaction between the metal nanoparticles and the carbon surface, which leads to inferior recyclability.<sup>39</sup> In order to satisfy the high standards of catalytic requirements, the introduction of heteroatoms has been further developed. Compared with pure mesoporous carbon, the introduction of heteroatoms can improve the physical characteristics of the support and simultaneously change the electronic characteristics of the active site.<sup>40,41</sup> The physical structure, surface properties, electronic structure of the active phase, and metal-support interaction of the catalyst are regulated by improving the preparation method and doping elements, and these factors promote the mass transfer rate of hydrogen and hydrogen dissociation adsorption performance which are conducive to achieving high catalytic activity and selectivity.<sup>42</sup>

In order to solve the dehalogenation of chemoselective catalytic hydrogenation and take both activity and cost into account, in this work we investigated a highly dispersed Ru nano-catalyst supported on a carrier of melamine and glucose by a simple one-step method. The reaction model selected was *p*-chloronitrobenzene (*p*-CNB) and the hydrogenation performances of catalysts with different carriers and preparation methods were systematically studied, and so the influence of carriers on active metals was analyzed. In addition, a mechanism for chemoselective hydrogenation of halogenated nitrobenzene was further probed.

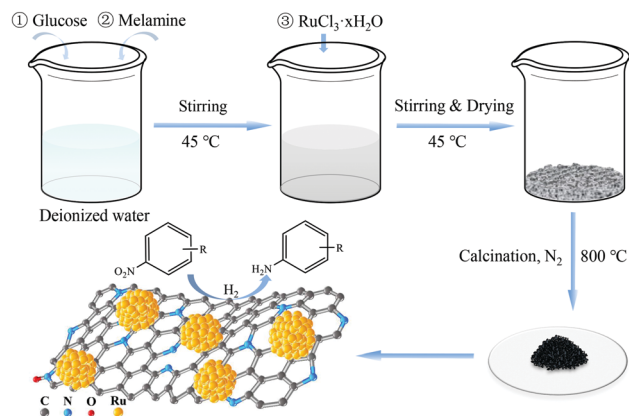
## 2. Experimental

### 2.1 Materials

Melamine (C.P.), glucose monohydrate (A.R.), anhydrous ethanol (A.R.),  $\text{RuCl}_3 \cdot x\text{H}_2\text{O}$ , and halogenated nitro compounds were purchased from Sinopharm Chemical Reagent Co. Ltd. The commercial 5% RuC catalyst, azoxybenzene, and *N*-phenylhydroxylamine were purchased from Aladdin Reagent Company. Deionized water was used as the solvent for all solutions.

### 2.2 Catalyst preparation

The Ru/CN catalyst was prepared by a simple one-pot pyrolysis process, as shown below. Firstly, the glucose (1 g) was dissolved in deionized water (40 mL) in a water bath at 45 °C. Then the melamine (20 g) was dispersed in the above solution with stirring for about 30 min until the suspension was well mixed. Finally, the ruthenium chloride aqueous solution (3.25 mL, Ru 0.0037 g mL<sup>-1</sup>) was added and the mixture was continuously stirred at 45 °C until the mixture had dried to grey solids.



Scheme 1 The preparation and application of the Ru/CN catalyst.

The grey solids were transferred into a drying oven for prolonged drying at 45 °C for 12 h, and then the solids were crushed and calcined in a tube furnace under the protection of high-purity nitrogen. The pyrolysis temperature was increased from ambient temperature to 350 °C, held for 2 h, and then increased to 800 °C at a heating rate of 5 °C min<sup>-1</sup>, and finally cooled down naturally to room temperature. In addition, to further test the superiority of the Ru/CN catalyst for the hydrogenation of halogenated nitroarenes, an Ru/C catalyst without the addition of nitrogen was obtained in a similar way. Scheme 1 reveals the preparation process and application of the catalyst.

In this work, an Ru/CN-imp catalyst as a comparison was prepared by the impregnation method. Firstly, the CN carrier was synthesized according to the previous process (Scheme 1) without the introduction of ruthenium. The CN carrier (0.55 g) was dispersed in deionized water (20 mL) under stirring at 45 °C. Then ruthenium chloride aqueous solution (3.25 mL, Ru 0.0037 g mL<sup>-1</sup>) was slowly dropped into the solution while the mixture was evaporated under stirring at 45 °C. Finally, the black powder was directly reduced at 200 °C (2 °C min<sup>-1</sup>) for 3 h in a 30 vol% H<sub>2</sub>/N<sub>2</sub> flow.

### 2.3 Catalyst characterization

The Ru content in the catalyst was analyzed by inductively coupled plasma atomic emission spectrometry (ICP-OES). The analysis of C and N elements in the catalyst was undertaken with an organic elemental analyzer (Vario Micro cube). Nitrogen absorption-desorption isotherms, BET specific surface areas, and pore size distribution curves were measured on a Micromeritics ASAP 2020 Sorptometer at -196 °C. The samples were degassed at 250 °C for 6 h before analysis. The specific surface areas ( $S_{\text{BET}}$ ) were determined using the Brunauer-Emmett-Teller (BET) method in a  $P/P_0$  range from 0.05 to 0.25. Pore size distribution curves were calculated using the desorption branch of the isotherms and the Barrett-Joyner-Halenda (BJH) method, and pore sizes ( $D_p$ ) were obtained from the peak positions of the distribution curves. Pore volume ( $V_p$ ) was taken at the  $P/P_0 = 0.990$  single point. A field emission scanning electron microscope (SEM, FEI Nova Nano SEM 450) was applied to

observe the catalyst morphology. X-ray diffraction (XRD) characterization was recorded on a Rigaku *D*/MAX-2200 diffractometer with Cu-K $\alpha$  radiation ( $\lambda = 0.1542$  nm) at a voltage of 40 kV and a current of 40 mA. Raman spectroscopy (InVia Reflex) with an Ar<sup>+</sup> ion laser (514.4 nm) as the excitation source was used to determine the degree of graphitization and defect level of the prepared materials. The size and distribution of the samples were studied with a field emission transmission electron microscope (TEM, JEOL JEM-2010F) operated at 200 kV. The samples were prepared by dropping an appropriate amount of the solution obtained after grinding and ultrasonically shaking the powder in ethanol onto copper mesh or microgrid (300 mesh) and then drying. The average particle sizes were calculated based on the average values of 200 particles in the TEM diagrams. The chemical composition and state of the sample surfaces were detected by an X-ray photoelectron spectrometer (XPS, ESCALAB 250Xi) with Al K $\alpha$  radiation ( $h\nu = 1486.6$  eV). The binding energy (BE) was calibrated against the C 1s signal (284.6 eV) of contaminant carbon.

#### 2.4 Catalytic hydrogenation

The hydrogenation of nitroarenes was conducted in a 100 mL stainless steel high-pressure tank reactor with an internal diameter of 45 mm with magnetic stirring. Before the series of experiments, we examined the effect of stirring rates on the catalytic activity for the hydrogenation of nitro aromatics under various reaction conditions including reaction temperature, substrate concentration and hydrogen pressure for the hydrogenation of *p*-CNB as a model compound over the Ru/CN catalyst. The results revealed that the catalytic activity showed little change when the stirring rate used was higher than 600 rpm; that is, the influencing factors of mass transfer of the reactants were eliminated in the reaction process.

The following reaction conditions were adopted to compare the activity of different catalysts: 2 mmol of *p*-CNB dissolved in 10 mL of anhydrous ethanol at 80 °C, 2 MPa (H<sub>2</sub>), and the appropriate amount of catalyst ( $[p\text{-CNB}]/[\text{metal}] = 1700$  (mol mol<sup>-1</sup>)). Before the reaction, the reactor was rinsed with 1 MPa H<sub>2</sub> 3 times to expel air from the reactor. In addition, when the temperature reached 80 °C, stirring of the reaction started at 800 rpm until the reaction stopped. Afterwards, the catalyst activity was calculated by the number of converted *p*-CNB moles per mole Ru per hour (TOF).

The recyclability of the Ru/CN catalyst was investigated using *p*-CNB as a model. In the cyclic reaction, 10 mmol of *p*-CNB was dissolved in 30 mL of anhydrous ethanol and 50 mg of Ru/CN catalyst was added into the reactor, and the reaction was performed for 1 h at 80 °C with 2 MPa (H<sub>2</sub>). After each reaction, the catalyst was recovered by filtration and washing with anhydrous ethanol three times and vacuum drying at room temperature. The loss of catalyst was inevitable during the washing process, and because of this, the ratio of *p*-CNB to Ru/CN was kept unchanged by adding fresh catalyst for each cycle test.

After the reaction, the resulting mixture was separated from the catalyst by filtration, diluted with anhydrous ethanol, and

then analyzed by gas chromatography-mass spectrometry (GC-MS, Shimadzu GCMS-QP 2010 Plus) and gas chromatography (GC, GC-9790) with a flame ionization detector and a capillary column (CP-SIL 5 CB, 30 m  $\times$  0.32 mm  $\times$  0.5  $\mu$ m).

### 3. Results and discussion

#### 3.1 Characterization of the catalyst

The actual Ru contents of the catalysts in Table 1 were measured by ICP-OES. The contents of Ru in the Ru/CN (2.40 wt%) and Ru/CN-imp (2.36 wt%) catalysts were similar, and the Ru content of the Ru/C catalyst (3.01 wt%) was higher because of the lack of N. In addition, the nitrogen contents in the CN carrier, Ru/CN, and Ru/CN-imp catalysts were 20.1 wt%, 19.8 wt% and 19.7 wt%, respectively. The nitrogen adsorption-desorption isotherms and the BJH pore size distributions of different catalysts are presented in Fig. 1. Similar to CN, the Ru/CN and Ru/CN-imp catalysts exhibited the apparent hysteresis loops of type IV adsorption isotherms (Fig. 1a), indicating typical mesoporous materials.<sup>43</sup> This result demonstrated that the doping with Ru did not change the pore structure of CN. Moreover, Table 1 also shows that the BET specific surface area, pore volume, and BJH

Table 1 Characterization results of different catalysts

Sample	Ru (wt%)	N (wt%)	$S_{\text{BET}}$ (m <sup>2</sup> g <sup>-1</sup> )	$V_p$ (cm <sup>3</sup> g <sup>-1</sup> )	$D_p$ (nm)
CN	—	20.1	414	0.97	3.8
Ru/C	3.01	—	118	0.01	2.0
Ru/CN	2.40	19.8	384	0.81	3.7
Ru/CN-imp	2.36	19.7	375	0.65	3.5

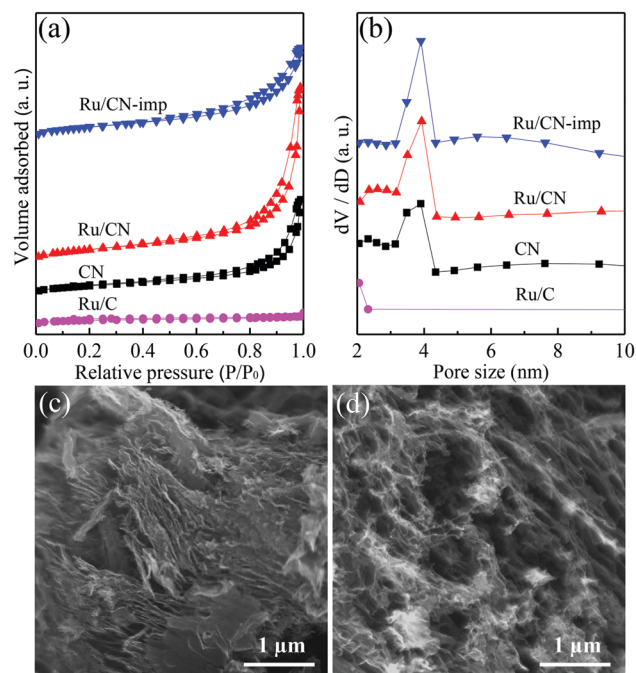


Fig. 1 (a) Nitrogen adsorption-desorption isotherms and (b) BJH pore size distributions of the Ru/C, CN, Ru/CN and Ru/CN-imp catalysts; (c) SEM images of Ru/C and (d) Ru/CN.

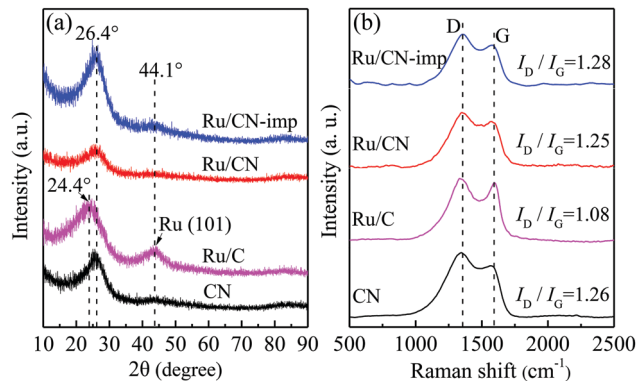


Fig. 2 (a) The wide-angle XRD patterns and (b) Raman spectra of the CN, Ru/C, Ru/CN and Ru/CN-imp catalysts.

pore size obviously increased with the addition of nitrogen in the order Ru/CN ( $384 \text{ m}^2 \text{ g}^{-1}$ ,  $0.81 \text{ cm}^3 \text{ g}^{-1}$ ,  $3.7 \text{ nm}$ ) > Ru/CN-imp ( $375 \text{ m}^2 \text{ g}^{-1}$ ,  $0.65 \text{ cm}^3 \text{ g}^{-1}$ ,  $3.5 \text{ nm}$ ) > Ru/C ( $118 \text{ m}^2 \text{ g}^{-1}$ ,  $0.01 \text{ cm}^3 \text{ g}^{-1}$ ,  $2.0 \text{ nm}$ ), but decreased slightly with the introduction of Ru, which might be related to the Ru loading in the pores. The catalyst structures observed from the SEM images in Fig. 1c and d could further verify the above results. Compared with the Ru/C catalyst, a loose and porous lamellar structure was more evident in the Ru/CN catalyst.

Fig. 2a displays the XRD patterns of CN and several catalysts. It is well known that the XRD peak of amorphous carbon is generally around  $25^\circ$ . After nitrogen doping, the weak and broad diffraction peak of the graphitic (002) (JCPDS 41-1487) shifted to a slightly higher value from  $24.4^\circ$  to  $26.4^\circ$  due to lattice distortion, which also demonstrated that the nitrogen atoms had been effectually doped into the graphitic system.<sup>44</sup> Compared with the Ru/C catalyst, which possessed an obvious diffraction peak of Ru (101) (JCPDS 06-0663) around  $2\theta = 44.1^\circ$ , the peaks of Ru in the Ru/CN and Ru/CN-imp catalysts were not obvious. This result indicated that the Ru particles of the N-doped catalysts were tiny and well dispersed, which could be attributed to the fact that N doping enhanced the interaction between Ru and the carrier, and effectively reduced the agglomeration of Ru clusters.<sup>45</sup>

Fig. 2b shows the Raman spectra, which reflected the chemical structures of the catalysts. The D peak ( $1350 \text{ cm}^{-1}$ ) is the feature of disorder-induction that corresponds to the impurity content and defect level in graphene, while the G peak ( $1580 \text{ cm}^{-1}$ ) which represents the complete structure of  $\text{sp}^2$  graphite is related to the degree of graphitization.<sup>46</sup> Hence  $I_D/I_G$  can be used as an indication of the amount of disorder and defects in graphene. Compared with the Ru/C catalyst ( $I_D/I_G = 1.08$ ), the  $I_D/I_G$  ratios of the CN carrier ( $I_D/I_G = 1.26$ ), Ru/CN catalyst ( $I_D/I_G = 1.25$ ), and Ru/CN-imp catalyst ( $I_D/I_G = 1.28$ ) were significantly larger after nitrogen doping under the same calcination temperature in an inert atmosphere, which indicated an increase in structural defects, such as sheet edges, due to the incorporation of nitrogen.

The microstructure of the catalysts was characterized by TEM, as shown in Fig. 3, and the average particle sizes were

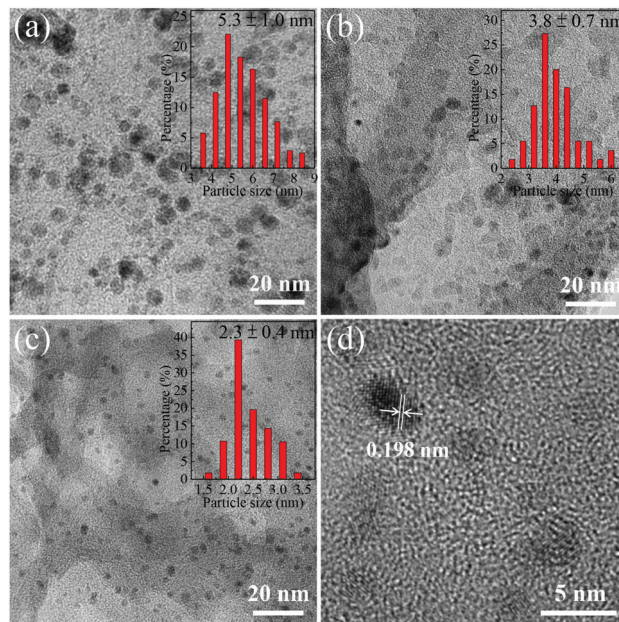


Fig. 3 TEM images and particle size distributions of (a) Ru/C, (b) Ru/CN-imp, (c) Ru/CN, and (d) HRTEM image of the Ru/CN catalyst.

calculated from about 200 particles. As shown in Fig. 3a–c, the particle size order was as follows: Ru/C ( $\sim 5.3 \text{ nm}$ ) > Ru/CN-imp ( $\sim 3.8 \text{ nm}$ ) > Ru/CN ( $\sim 2.3 \text{ nm}$ ). It was found that the Ru particles of the catalysts doped with nitrogen were much smaller and more homogeneously-distributed than those without nitrogen, which was consistent with the XRD results. This phenomenon was attributed to the interactions between the N and Ru limiting the overgrowth and aggregation of particles. The Ru particle size of the Ru/CN catalyst prepared by the one-pot pyrolysis method was smaller than that of the impregnated Ru/CN-imp catalyst due to the stronger interaction between N and Ru. Besides, the HRTEM images in Fig. 3d indicated that the particles in the Ru/CN catalyst exhibited a lattice distance of  $0.198 \text{ nm}$ , attributed to the (101) crystal faces of the hcp Ru crystallites.

XPS analysis was performed to identify the composition and electronic structure of the catalysts, and the C, N, O, and Ru elements of the Ru/CN catalyst were detected in the XPS full spectrum (Fig. S1, ESI†). Fig. 4 exhibits the XPS spectra of N and Ru of the prepared catalysts. As shown in Fig. 4a, the N 1s peaks of the CN and Ru/CN catalysts could be divided into four peaks at  $397.7 \text{ eV}$  ( $398.0 \text{ eV}$ ),  $399.0 \text{ eV}$  ( $399.3 \text{ eV}$ ),  $400.3 \text{ eV}$  ( $400.5 \text{ eV}$ ), and  $402.6 \text{ eV}$ , representing pyridinic-N, pyrrolic-N, graphitic-N and pyridinic N-oxide, respectively,<sup>44</sup> and pyridinic-N and graphitic-N were in the majority. These types of N indicated the successful introduction of nitrogen-containing functional groups into the carbon grid of graphene.<sup>47</sup> Moreover, it is worth mentioning that the N 1s peaks of the Ru/CN shifted to slightly higher binding energy after the Ru mixing. Fig. 4b displays the peaks of Ru 3p of the Ru/C and Ru/CN catalysts at  $462.8 \text{ eV}$  ( $462.6 \text{ eV}$ ) and  $485.1 \text{ eV}$  ( $484.8 \text{ eV}$ ) with a slight shift to lower binding energy after nitrogen doping, corresponding to  $\text{Ru}^0 3\text{p}_{3/2}$  and  $\text{Ru}^0 3\text{p}_{1/2}$ .<sup>48</sup> Both the shift to higher binding energy of N

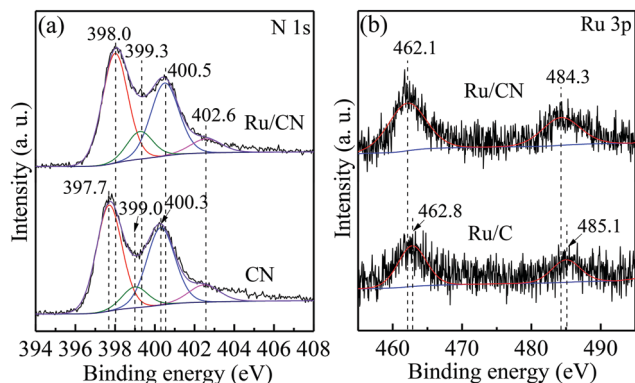


Fig. 4 XPS spectra of the prepared catalysts: (a) N 1s and (b) Ru 3p.

and the shift to lower binding energy of Ru clearly demonstrated that the interaction between N and Ru led to electron transfer from N to Ru.

### 3.2 Catalytic reaction

The *p*-CNB was used as a typical sample to estimate the catalyst performance on the selective reduction of halogenated nitroarenes, and the reaction results of different catalysts are shown in Table 2. It was clearly demonstrated that the CN carrier was inactive, and all of the Ru catalysts obtained by *in situ* pyrolysis exhibited a certain conversion of *p*-CNB and *p*-CAN selectivity, higher than that of the commercial 5% RuC catalysts. Compared with Ru/C, Ru/CN showed much higher *p*-CNB conversion (13.2% vs. 1.7%) and TOF (1333 h<sup>-1</sup> vs. 171 h<sup>-1</sup>). It could be concluded that the N doping not only improved the pore structure and Ru particle dispersion, as shown in Table 1 and Fig. 1–3, but also promoted the hydrogenation of *p*-CNB on the catalyst surface, leading to high catalytic activity. The higher *p*-CAN selectivity of the Ru/CN catalyst might be caused by the combination of factors including larger surface area and pore size, and the interactions between N and Ru, which contributed to deep hydrogenation of the hydroxyaniline intermediate to amine (note: no dehalogenated aniline was detected over Ru/CN). The preparation method also strongly affected the hydrogenation of *p*-CNB. The Ru/CN catalyst obtained by one-pot pyrolysis exhibited obviously higher catalytic activity and selectivity of *p*-CAN than the Ru/CN-imp catalyst likely due to different interactions between N and Ru particles. Fig. S2 (ESI<sup>†</sup>) shows the influence of reaction

Table 2 Hydrogenation reduction of *p*-CNB to *p*-CAN over several catalysts<sup>a</sup>

Entry	Cat.	Conv. <sup>b</sup> (%)	Sel. <sup>c</sup> (%)	TOF <sup>d</sup> (h <sup>-1</sup> )
1	CN	0	0	0
2	Ru/C	1.7	96.7	171
3	Ru/CN	13.2	100	1333
4	Ru/CN-imp	3.9	98.4	394
5	5% RuC	1.5	95.1	152

<sup>a</sup> Reaction conditions: 2 mmol of *p*-CNB, [*p*-CNB]/[metal] = 1700 (mol/mol), 10 mL of anhydrous ethanol, 80 °C, 2 MPa H<sub>2</sub>, 800 rpm. <sup>b</sup> Conversion at 10 min. <sup>c</sup> Selectivity of *p*-CAN at 100% conversion of *p*-CNB. <sup>d</sup> The number of moles of *p*-CNB converted per mole of Ru per hour.

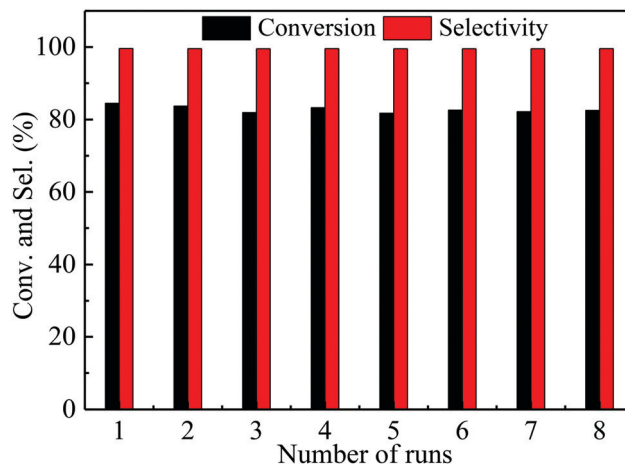


Fig. 5 Reusable properties of the Ru/CN catalyst for hydrogenation of *p*-CNB to *p*-CAN. Reaction conditions: 10 mmol of *p*-CNB, 30 mL of anhydrous ethanol, 50 mg of Ru/CN catalyst, 2 MPa H<sub>2</sub>, 80 °C, 1 h, 800 rpm.

temperature and pressure on the performance of the Ru/CN catalyst, revealing that the effect of temperature on activity was obviously greater than that of pressure.

After the catalyst comparison experiments, cyclic hydrogenation experiments on *p*-CNB were performed to evaluate the recyclability of the Ru/CN catalyst. The reaction results of *p*-CNB hydrogenation to *p*-CAN in Fig. 5 were almost identical either in activity or selectivity after 8 cycles. This result revealed that the Ru/CN catalyst had superior stability. As we all know, leaching and growth of active metal are the major problems for the deactivation of a catalyst. Nevertheless, the active metal Ru was not detected in the liquid after the reaction, and the Ru content of the spent Ru/CN catalyst by ICP analysis was 2.38 wt%, similar to that of the fresh catalyst (2.40 wt%), showing almost no loss of Ru. In addition, the pore structure of the spent Ru/CN catalyst in Fig. 6a and b remained nearly unchanged with an average pore size of 3.8 nm and pore volume of 0.79 cm<sup>3</sup> g<sup>-1</sup>, compared with that of the fresh catalyst in Table 1. This result indicated that the catalyst possessed good structural stability and the pore structure was not destroyed during the reaction. The particle size distribution of Ru (Fig. 6c) with an average particle size of 2.3 nm and the chemical state of Ru (Fig. 6d) were similar to those of the fresh catalyst in Fig. 3 and 4, further indicating the superb physical and chemical stability of the Ru/CN catalyst for the hydrogenation of halogenated nitroarenes.

In order to prove the general applicability of Ru/CN catalyst for the hydrogenation of other halogenated nitroarenes, the substrates in Table 3 were tested for the hydrogenation reaction. It is noteworthy to mention that no obvious dehalogenated product was detected during the hydrogenation of halogenated nitroarenes to corresponding haloanilines including the multiple identical or different halogen groups of -F, -Cl or -Br (entries 5–8, Table 3). That was a significant advantage over many highly active but dehalogenating catalysts: for instance, the noble metal catalysts of Pt and Pd. In the presence of electron-donating groups such as -CH<sub>3</sub>, -NH<sub>2</sub> (entries 9–12, Table 3)

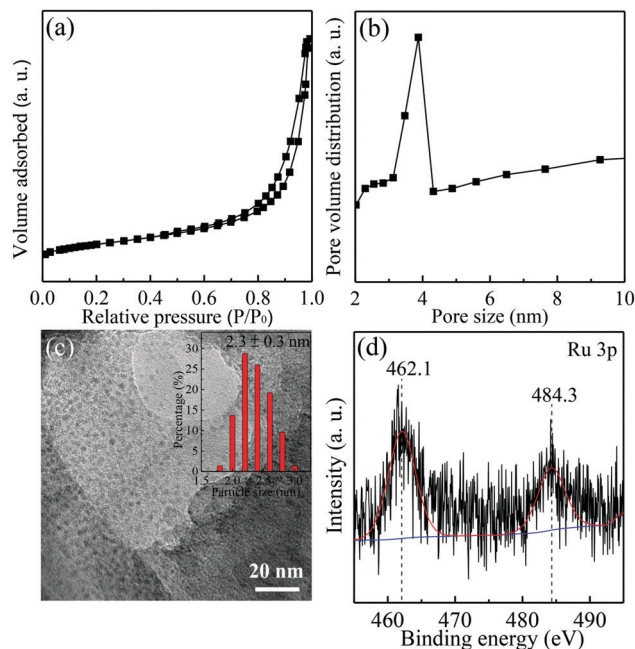


Fig. 6 Characterization of the spent Ru/CN catalyst: (a) nitrogen adsorption-desorption isotherms, (b) pore size distribution, (c) TEM image and particle size distribution, and (d) Ru 3p XPS spectra.

and electron-withdrawing groups including -F, -Cl and -Br (Table 3) which were more easily reduced they also showed an outstanding selectivity (>99.6%). Remarkably, some substrates with double or triple bonds (entries 13 and 14, Table 3) and nitrogen-containing heterocycles (entries 15–17, Table 3) were successfully reduced to the corresponding haloanilines without almost any byproducts. Factors for the hydrogenation activity of halogenated nitroarenes are complex, including the electronic effect with groups and the conjugated effect of multiple groups. The sequence of catalytic activity in the halogen groups with different electronegativities at the same position was as follows: -F > -Cl > -Br (entries 1 and 4–6, Table 3), and in general, the activity of hydrogenation in the *para*-position of the same group was greater than that in the *ortho*-position or *meta*-position (entries 1–3, Table 3) which could be ascribed to the halogens in the *para*-position making the polarity of N=O stronger. Moreover, for the unsaturated groups such as carbonyl groups (C=O, entry 14, Table 3) which were easily hydrogenated,<sup>49</sup> the catalyst still exhibited a high selectivity of nearly 100%.

The mechanism of the hydrogenation reduction of aromatic nitro compounds is rather complicated and, among many related studies, the two reaction paths of the direct and indirect reactions proposed by Haber are generally accepted.<sup>50</sup> In the previous reaction, we found that when the reaction was incomplete, the selectivity of *p*-CAN did not reach the highest level, and the selectivity increased with the conversion. Therefore, the products were analyzed after the reaction by GCMS, and the intermediates of hydroxyaniline and azoxybenzene were detected in the products, as shown in Fig. 7. The content of hydroxyaniline was much higher than that of azoxybenzene, and their yields increased first and then decreased as the reaction proceeded.

Table 3 The selective hydrogenation of various halogenated nitroarenes to corresponding amines over the Ru/CN catalyst<sup>a</sup>

Entry	Substrate	Time (min)	Conv. (%)	Sel. (%)	TOF <sup>b</sup> (h <sup>-1</sup> )
1		90	100	100	1333
2		140	100	100	984
3		150	100	100	930
4		135	100	100	1060
5		120	100	99.8	1194
6		115	100	100	1208
7		120	100	100	1159
8		60	100	100	1923
9		150	100	100	956
10		165	100	100	918
11		150	100	100	956
12		420	100	99.7	285
13		210	100	99.7	493
14		150	100	100	957
15		120	100	99.6	1211
16		75	100	100	1777
17		390	100	100	313

<sup>a</sup> Reaction conditions: 2 mmol of the substrate, 10 mg of Ru/CN catalyst, 10 mL of anhydrous ethanol, 80 °C, 2 MPa H<sub>2</sub>, 800 rpm. <sup>b</sup> TOF: the TOF value is calculated based on total metal and initial conversions of less than 15%.

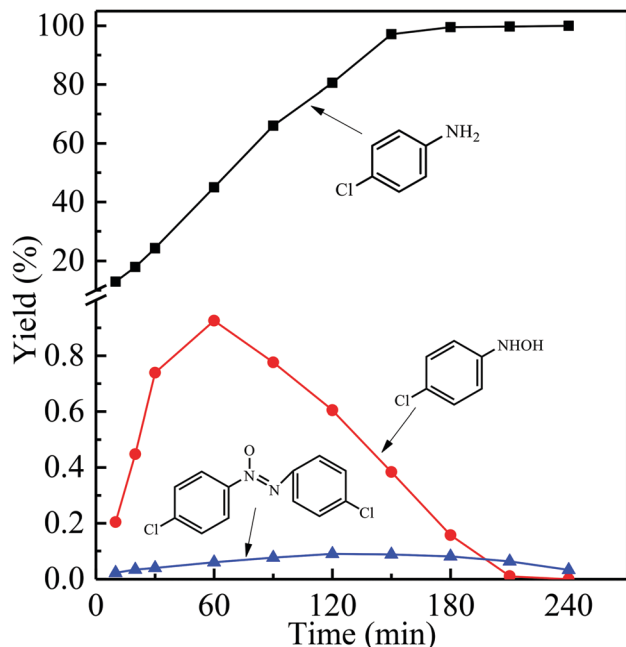


Fig. 7 The yield of each product in the hydrogenation of *p*-CNB over the Ru/CN catalyst, including *p*-CAN, hydroxyaniline and azoxybenzene. Reaction conditions: 10 mmol of *p*-CNB, 25 mg of Ru/CN catalyst, 10 mL of anhydrous ethanol, 80 °C, 2 MPa H<sub>2</sub>, 800 rpm.

Therefore, it was speculated that the two reaction paths existed simultaneously in the hydrogenation of halogenated nitroarenes to corresponding haloanilines over an Ru catalyst. In order to further verify this, experiments were conducted on the intermediates of hydroxyaniline and azoxybenzene respectively and it was found that both intermediates could be hydrogenated, but the reaction rate of hydroxyaniline (100%) was much faster than that of azoxybenzene (35.4%) under the same reaction conditions.

The two reaction paths were obtained, as shown in Fig. 8, and the direct path was dominant. The reduction of nitro to nitroso and further reduction to hydroxylamine happened rapidly, while the main rate-controlling step of nitro reduction to amino was the reduction of hydroxylamine to aniline. Furthermore, the indirect path took place in a series of consecutive steps through the condensation of nitroso and hydroxyaniline to azoxybenzene and further hydrogenation to azobenzene, phenylhydrazine, and aniline.

It was concluded that the synergistic effect between the mixed N and the active metal Ru not only accelerated the dissociation of hydrogen on Ru, but also increased the amount of electron-rich hydrogen. Attributed to the nucleophilic substitution reaction of the nitro reduction,<sup>51</sup> the more electron-rich hydrogen is conducive to the reduction of the nitro group. Meanwhile, the electronegative halogen is vulnerable to attack by hydrogen in an electron-poor state. So that hydrogen in a more electron-rich state can exactly inhibit the hydrogen dissolution of an R-C bond, in which case the dehalogenation is depressed to a certain degree and the chemical selectivity is significantly improved.

## 4. Conclusions

In this study, highly chemoselective Ru/CN nanocomposites with superfine and uniformly dispersed Ru nanoparticles were successfully synthesized by a simple one-pot pyrolysis method. The Ru/CN catalyst exhibited good activity and superior selectivity in the hydrogenation of various halogenated nitroarenes to corresponding haloanilines with almost 100% selectivity of the complete conversion. The interaction between N and Ru promoted the production of hydrogen in an electron-rich state, and thus accelerated the reduction of the nitro group and effectively reduced the dehalogenation. Moreover, it was

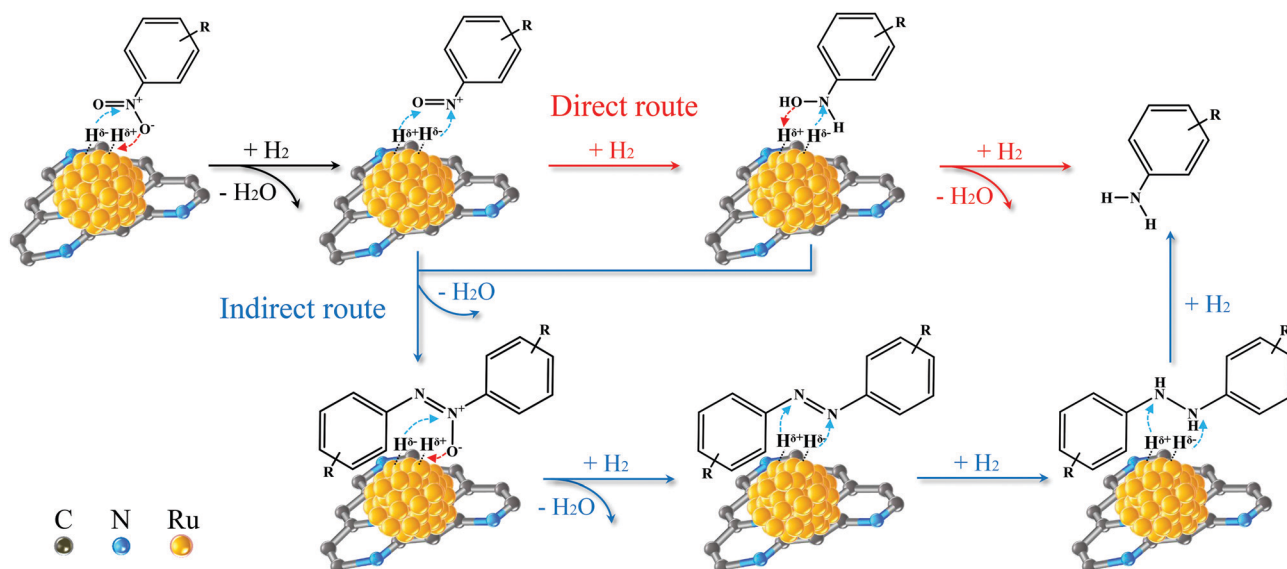


Fig. 8 The reaction routes of the Ru/CN catalyst for the hydrogenation of halogenated nitroarenes.

demonstrated that two pathways, direct and indirect, existed simultaneously in the hydrogenation of halogenated nitroarenes over the Ru/CN catalyst, and the direct pathway dominated.

## Conflicts of interest

There are no conflicts to declare.

## Acknowledgements

This research was supported by the Shanghai Engineering Research Center of Green Energy Chemical Engineering (No. 18DZ2254200).

## Notes and references

- I. Sorribes, L. C. Liu and A. Corma, *ACS Catal.*, 2017, 7, 2698–2708.
- S. Zhang, C. R. Chang, Z. Q. Huang, J. Li, Z. M. Wu, Y. Y. Ma, Z. Y. Zhang, Y. Wang and Y. Q. Qu, *J. Am. Chem. Soc.*, 2016, 138, 2629–2637.
- R. V. Jagadeesh, G. Wienhöfer, F. A. Westerhaus, A. E. Surkus, M. M. Pohl, H. Junge, K. Junge and M. Beller, *Chem. Commun.*, 2011, 47, 10972–10974.
- Y. Markushyna, C. Teutloff, B. Kurpil, D. Cruz, I. Lauer mann, Y. Zhao, M. Antonietti and A. Savateev, *Appl. Catal., B*, 2019, 248, 211–217.
- Q. H. Yang, Y. Z. Chen, Z. U. Wang, Q. Xu and H. L. Jiang, *Chem. Commun.*, 2015, 51, 10419–10422.
- W. Zhang, W. Wu, Y. Long, F. S. Wang and J. T. Ma, *J. Colloid Interface Sci.*, 2018, 522, 217–227.
- Z. Liu, W. H. Dong, S. S. Cheng, S. Guo, N. Z. Shang, S. T. Gao, C. Feng, C. Wang and Z. Wang, *Catal. Commun.*, 2017, 95, 50–53.
- X. Cui, Q. Zhang, M. Tian and Z. Dong, *New J. Chem.*, 2017, 41, 10165–10173.
- K. Junge, B. Wendt, N. Shaikh and M. Beller, *Chem. Commun.*, 2010, 46, 1769–1771.
- N. M. Ivanova, Y. A. Visurkhanova, E. A. Soboleva and S. O. Kenzhetaeva, *Electrochem. Commun.*, 2018, 96, 66–70.
- L. C. Liu, F. Gao, P. Concepción and A. Corma, *J. Catal.*, 2017, 350, 218–225.
- S. M. Baghbanian, M. Farhang, S. M. Vahdat and M. Tajbakhsh, *J. Mol. Catal. A: Chem.*, 2015, 407, 128–136.
- P. Serna and A. Corma, *ACS Catal.*, 2015, 5, 7114–7121.
- F. Q. He, X. H. Deng and M. Chen, *Fuel*, 2017, 199, 523–531.
- D. Shah and H. Kaur, *J. Mol. Catal. A: Chem.*, 2014, 381, 70–76.
- B. B. Huang, J. Li, X. K. Cao, Y. Y. Zhu, W. Q. Chen and C. Lei, *Electrochim. Acta*, 2019, 296, 980–988.
- A. Grirrane, A. Corma and H. García, *Science*, 2008, 322, 1661–1664.
- L. Huang, Y. Lv, S. T. Wu, P. L. Liu, W. Xiong, F. Hao and H. A. Luo, *Appl. Catal., A*, 2019, 577, 76–85.
- J. J. Song, Z. F. Huang, L. Pan, K. Li, X. W. Zhang, L. Wang and J. J. Zou, *Appl. Catal., B*, 2018, 227, 386–408.
- Q. F. Wu, B. Zhang, C. Zhang, X. C. Meng, X. Su, S. Jiang, R. H. Shi, Y. Li, W. W. Lin, M. Arai, H. Y. Cheng and F. Y. Zhao, *J. Catal.*, 2018, 364, 297–307.
- P. Jing, T. Gan, H. Qi, B. Zheng, X. F. Chu, G. Y. Yu, W. F. Yan, Y. C. Zou, W. X. Zhang and G. Liu, *Chin. J. Catal.*, 2019, 40, 214–222.
- P. Zhou, D. Z. Li, S. W. Jin, S. H. Chen and Z. H. Zhang, *Int. J. Hydrogen Energy*, 2016, 41, 15218–15224.
- K. Halder, G. Bengtson, V. Filiz and V. Abetz, *Appl. Catal., A*, 2018, 555, 178–188.
- J. J. Martínez, E. X. Aguilera, J. Cubillos, H. Rojas, A. Gómez-Cortés and G. Díaz, *Mol. Catal.*, 2019, 465, 54–60.
- N. Salam, B. Banerjee, A. S. Roy, P. Mondal, S. Roy, A. Bhaumik and S. M. Islam, *Appl. Catal., A*, 2014, 477, 184–194.
- S. Dayan, F. Arslan and N. O. Kalaycioglu, *Appl. Catal., B*, 2015, 164, 305–315.
- C. J. Jiang, Z. Y. Shang and X. H. Liang, *ACS Catal.*, 2015, 5, 4814–4818.
- C. Yu, J. J. Fu, M. Muzzio, T. L. Shen, D. Su, J. J. Zhu and S. H. Sun, *Chem. Mater.*, 2017, 29, 1413–1418.
- R. V. Jagadeesh, D. Banerjee, P. B. Arockiam, H. Junge, K. Junge, M. M. Pohl, J. Radnik, A. Brückner and M. Beller, *Green Chem.*, 2015, 17, 898–902.
- A. Goswami, R. G. Kadam, J. Tuček, Z. Sofer, D. Bouša, R. S. Varma, M. B. Gawande and R. Zbořil, *Chem. Eng. J.*, 2020, 382, 122469.
- C. F. Zhang, J. M. Lu, M. R. Li, Y. H. Wang, Z. Zhang, H. J. Chen and F. Wang, *Green Chem.*, 2016, 18, 2435–2442.
- V. Marakatti and S. Peter, *New J. Chem.*, 2016, 40, 5448–5457.
- H. G. Huang, X. C. Liang, X. G. Wang, Y. Sheng, C. J. Chen, X. J. Zou and X. G. Lu, *Appl. Catal., A*, 2018, 559, 127–137.
- T. B. Shi, H. Li, L. H. Yao, W. J. Ji and C. T. Au, *Appl. Catal., A*, 2012, 425–426, 68–73.
- P. Mariusz, *Curr. Org. Synth.*, 2012, 9, 470–487.
- J. P. Xiao, X. L. Pan, F. Zhang, H. B. Li and X. H. Bao, *Chem. Sci.*, 2017, 8, 278–283.
- P. D. A. Patra, A. Dutta and A. Bhaumik, *Catal. Commun.*, 2010, 651–655.
- R. M. Mironenko, O. B. Belskaya, T. I. Gulyaeva, M. V. Trenikhin and V. A. Likholobov, *Catal. Commun.*, 2018, 114, 46–50.
- X. Xu, Y. Li, Y. T. Gong, P. F. Zhang, H. R. Li and Y. Wang, *J. Am. Chem. Soc.*, 2012, 134, 16987–16990.
- J. Li, X. Zhou, N. Z. Shang, C. Feng, S. T. Gao and C. Wang, *New J. Chem.*, 2018, 42, 16823–16828.
- Y. B. Sun, C. Y. Cao, C. Liu, J. Liu, Y. N. Zhu, X. S. Wang and W. G. Song, *Carbon*, 2017, 125, 139–145.
- A. M. Alexander and J. S. J. Hargreaves, *Chem. Soc. Rev.*, 2010, 39, 4388–4401.
- M. Tan, X. Wang, X. Shang, X. Zou, X. Lu and W. Ding, *J. Catal.*, 2014, 314, 117–131.
- F. Yang, C. Chi, C. X. Wang, Y. Wang and Y. F. Li, *Green Chem.*, 2016, 18, 4254–4262.

- 45 J. F. Liang, X. M. Zhang, L. Y. Jing and H. Q. Yang, *Chin. J. Catal.*, 2017, **38**, 1252–1260.
- 46 J. L. Long, X. Q. Xie, J. Xu, Q. Gu, L. M. Chen and X. X. Wang, *ACS Catal.*, 2012, **2**, 622–631.
- 47 W. Qian, L. N. Lin, Y. X. Qiao, X. G. Zhao, Z. C. Xu, H. H. Gong, D. F. Li, M. Y. Chen, R. Huang and Z. S. Hou, *Appl. Catal., A*, 2019, **585**, 117183.
- 48 J. V. Rojas, M. Toro-Gonzalez, M. C. Molina-Higgins and C. E. Castano, *Mater. Sci. Eng., B*, 2016, **205**, 28–35.
- 49 W. L. Wu, J. W. Li, Z. Y. Chen, W. Z. Chen, H. S. Pang, K. B. Ma and J. Zeng, *J. Catal.*, 2019, **373**, 209–214.
- 50 Z. F. Haber, *Elektrochem*, 1898, **4**, 506.
- 51 G. D. Yadav and M. R. Kharkara, *Appl. Catal., A*, 1995, **126**, 115–123.